Super$B$ Detector
Technical Design Report

Abstract

This report describes the technical design detector for Super$B$.

E. Grauges,
Universitat De Barcelona, *Fac. Fisica. Dept. ECM Barcelona E-08028, Spain*

G. Donvito, V. Spinoso
INFN Bari *and* **Università di Bari,** *Dipartimento di Fisica, I-70126 Bari, Italy*

M. Manghisoni, V. Re, G. Traversi
INFN Pavia *and* **Università di Bergamo** *Dipartimento di Ingegneria Industriale, I-24129 Bergamo, Italy*

G. Eigen, D. Fehlker, L. Helleve
University of Bergen, *Institute of Physics, N-5007 Bergen, Norway*

A. Carbone, R. Di Sipio, A. Gabrielli, D. Galli, F. Giorgi, C. Grandi, U. Marconi, S. Perazzini, C. Sbarra, V. Vagnoni, S. Valentinetti, M. Villa, A. Zoccoli
INFN Bologna *and* **Università di Bologna,** *Dipartimento di Fisica, I-40127 Bologna, Italy*

C. Cheng, A. Chivukula, D. Doll, B. Echenard, D. Hitlin, P. Ongmongkolkul, F. Porter, A. Rakitin, M. Thomas, R. Zhu
California Institute of Technology, *Pasadena, California 91125, USA*

G. Tatishvili
Carleton University, *Ottawa, Ontario, Canada K1S 5B6*

R. Andreassen, C. Fabby, B. Meadows, A. Simpson, M. Sokoloff, K. Tomko
University of Cincinnati, *Cincinnati, Ohio 45221, USA*

M. Andreotti, W. Baldini, R. Calabrese, V. Carassiti, G. Cibinetto, A. Cotta Ramusino, A. Gianoli, E. Luppi, E. Luppi, M. Munerato, L. Tomassetti
INFN Ferrara *and* **Università di Ferrara,** *Dipartimento di Fisica, I-44100 Ferrara, Italy*

D. Stoker
University of California, Irvine *Irvine, California 92697, USA*

O. Bezshyyko, G. Dolinska
Taras Shevchenko National University of Kyiv *Kyiv, 01601, Ukraine*

N. Arnaud, C. Beigbeder, F. Bogard, D. Breton, L. Burmistrov, D. Charlet, A. El Berni, J. Maalmi, V. Puill, A. Stocchi, V. Tocut, S. Wallon, G. Wormser
Laboratoire de l'Accélérateur Linéaire, *IN2P3/CNRS, Université Paris-Sud 11, F-91898 Orsay, France*

J.-F. Muraz, J.-S. Real
Laboratoire de Physique Subatomique et Cosmologie, *IN2P3/CNRS, Université Joseph Fourier Grenoble 1 & Institut Polytechnique de Grenoble, 53 rue des Martyrs F-38026 Grenoble Cedex, France*

D. Brown
Lawrence Berkeley National Laboratory, *University of California, Berkeley, California 94720, USA*

A. Calcaterra, R. de Sangro, G. Felici, G. Finocchiaro, P. Patteri, I. Peruzzi, M. Piccolo,
M. Rama
Laboratori Nazionali di Frascati dell'INFN, *I-00044 Frascati, Italy*

S. Fantinel, G. Maron
Laboratori Nazionali di Legnaro dell'INFN, *I-35020 Legnaro, Italy*

E. Ben-Haim, G. Calderini, G. Marchiori
Laboratoire de Physique Nucléaire et de Hautes Energies, *IN2P3/CNRS, Université
Pierre et Marie Curie-Paris 6, F-75005 Paris, France*

R. Cenci, A. Jawahery, D.A. Roberts
University of Maryland, *College Park, Maryland 20742, USA*

D. Lindemann, P. Patel, S. Robertson, D. Swersky
McGill University, *Montréal, Québec, Canada H3A 2T8*

P. Biassoni, M. Citterio, V. Liberali, F. Palombo, A. Stabile, S. Stracka
INFN Milano *and* **Università di Milano,** *Dipartimento di Fisica, I-20133 Milano, Italy*

A. Aloisio, G. De Nardo, A. Doria, R. Giordano, A. Ordine, S. Pardi, G. Russo, C. Sciacca
INFN Napoli *and* **Università di Napoli Federico II,** *Dipartimento di Scienze Fisiche,
I-80126, Napoli, Italy*

A.Y. Barniakov, M.Y. Barniakov, V.E. Blinov, V.P. Druzhinin, V.B.. Golubev, S.A. Kononov,
E. Kravchenko, A.P. Onuchin, S.I. Serednyakov, Y.I. Skovpen, E.P. Solodov
Budker Institute of Nuclear Physics, *Novosibirsk 630090, Russia*

M. Bellato, M. Benettoni, M. Corvo, A. Crescente, F. Dal Corso, C. Fanin, E. Feltresi,
N. Gagliardi, S. Longo, M. Morandin, M. Posocco, M. Rotondo, G. Simi, R. Stroili
INFN Padova *and* **Università di Padova,** *Dipartimento di Fisica, I-35131 Padova, Italy*

C. Andreoli, L. Gaioni, E. Pozzati, L. Ratti, V. Speziali
INFN Pavia *and* **Università di Pavia,** *Dipartimento di Elettronica, I-27100 Pavia, Italy*

D. Aisa, M. Bizzarri, C. Cecchi, S. Germani, P. Lubrano, E. Manoni, A. Papi, A. Piluso , A. Rossi
INFN Perugia *and* **Università di Perugia,** *Dipartimento di Fisica, I-06123 Perugia, Italy*

M. Lebeau
INFN Perugia, *I-06123 Perugia, Italy, and*
California Institute of Technology, *Pasadena, California 91125, USA*

A. Fella
INFN Pisa *I-56124 Pisa, Italy and* **Laboratoire de l'Accélérateur Linéaire,** *IN2P3/CNRS,
Université Paris-Sud 11, F-91898 Orsay, France and* **Università di Ferrara,** *Dipartimento di
Fisica, I-44100 Ferrara, Italy*

C. Avanzini, G. Batignani, S. Bettarini, F. Bosi, M. Ceccanti, A. Cervelli, A. Ciampa,
F. Crescioli, M. Dell'Orso, D. Fabiani, F. Forti, P. Giannetti, M. Giorgi, S. Gregucci, A. Lusiani,
P. Mammini, G. Marchiori, M. Massa, E. Mazzoni, F. Morsani, N. Neri, E. Paoloni,
L. Perez Perez, M. Piendibene, A. Profeti, G. Rizzo, L. Sartori, J. Walsh, E. Yurtsev
INFN Pisa, Università di Pisa, *Dipartimento di Fisica, and* **Scuola Normale Superiore,**
I-56127 Pisa, Italy

D.M. Asner, J. E. Fast, R.T. Kouzes,
Pacific Northwest National Laboratory, *Richland, Washington 99352, USA*

A. Bevan, F. Gannaway, J. Mistry, C. Walker
Queen Mary, *University of London, London E1 4NS, United Kingdom*

C.A.J. Brew, R.E. Coath, J.P. Crooks, R.M. Harper, A. Lintern, A. Nichols, M. Staniztki,
R. Turchetta, F.F. Wilson
Rutherford Appleton Laboratory, *Chilton, Didcot, Oxon, OX11 0QX, United Kingdom*

V. Bocci, G. Chiodi, R. Faccini, C. Gargiulo, D. Pinci, L. Recchia, D. Ruggieri
INFN Roma *and* **Università di Roma La Sapienza,** *Dipartimento di Fisica, I-00185 Roma,*
Italy

A. Di Simone
INFN Roma Tor Vergata *and* **Università di Roma Tor Vergata,** *Dipartimento di Fisica,*
I-00133 Roma, Italy

P. Branchini, A. Passeri, F. Ruggieri, E. Spiriti
INFN Roma Tre *and* **Università di Roma Tre,** *Dipartimento di Fisica, I-00154 Roma, Italy*

D. Aston, M. Convery, G. Dubois-Felsmann, W. Dunwoodie, M. Kelsey, P. Kim, M. Kocian,
D. Leith, S. Luitz, D. MacFarlane, B. Ratcliff, M. Sullivan, J. Va'vra, W. Wisniewski, W. Yang
SLAC National Accelerator Laboratory *Stanford, California 94309, USA*

K. Shougaev, A. Soffer
School of Physics and Astronomy, Tel Aviv University *Tel Aviv 69978, Israel*

F. Bianchi, D. Gamba, G. Giraudo, P. Mereu
INFN Torino *and* **Università di Torino,** *Dipartimento di Fisica Sperimentale, I-10125*
Torino, Italy

G. Dalla Betta, G. Fontana, G. Soncini
INFN Padova *and* **Università di Trento,** *ICT Department, I-38050 Trento, Italy*

M. Bomben, L. Bosisio, P. Cristaudo, G. Giacomini, D. Jugovaz, L. Lanceri, I. Rashevskaya,
G. Venier, L. Vitale
INFN Trieste *and* **Università di Trieste,** *Dipartimento di Fisica, I-34127 Trieste, Italy*

R. Henderson
TRIUMF *Vancouver, British Columbia, Canada V6T 2A3*

J.-F. Caron, C. Hearty, P. Lu, R. So
University of British Columbia, *Vancouver, British Columbia, Canada V6T 1Z1*

P. Taras
Université de Montreál, *Physique des Particules, Montreál, Québec, Canada H3C 3J7*

A. Agarwal, J. Franta, J.M. Roney
University of Victoria, *Victoria, British Columbia, Canada V8W 3P6*

Contents

1 Instrumented Flux Return

1.1 Physics Requirements and Performance Goals

Calabrese, Lesiak, Cibinetto (3, 4 pages)

The principal task of the Instrumental Flux Return (IFR) detector is the detection of muons and neutral hadrons. These goals are realized in in the large iron structure, needed as the magnet return yoke.

Muons are considered as important messengers of New Physics (NP) in the processes like $b \rightarrow s\mu^+\mu^-$, $\tau \rightarrow \mu\gamma$, $\tau^+ \rightarrow \mu^+\mu^-\mu^+$, $\tau \rightarrow \mu X$, $X = \rho, \eta^{(\prime)}, f_0...$, $B_s \rightarrow \mu^+\mu^-$, $D^0 \rightarrow \mu^+\mu^-$, to name but a few [?], [?]. Moreover, their detection is crucial in a substantial part of studies related to the determination of sides and angles of the unitarity triangle which are based on semileptonic decays of B mesons. Also, in these decays, the sign of the lepton charge determines the flavour of the parent heavy meson, thus providing one of the tags for the CP-asymmetry measurements.

The IFR will also act as hadronic calorimeter, thus providing the detection of neutral hadrons. Among the latter, special attention is paid to the K_L^0 mesons reconstruction, which is realized in conjunction with the information provided by the electromagnetic calorimeter. The ability to reconstruct the K_L^0s allows, in particular, to compare CP-violation effects in the decay channel $B \rightarrow J/\psi K_L^0$ with those in $B \rightarrow J/\psi K_S^0$.

1.2 Detector Overview

1.2.1 The Absorber Structure

Posocco, Benettoni (2 pages)

The SuperB Flux Return structure, used as absorber material to identify muons, will be composed by an hexagonal iron yoke constituted by a barrel and two endcaps (see fig. 1.1). Each of the two endcaps is, in turn, composed by two doors, while the barrel is composed by six sectors called sextants. All the main parts are made of welded steel plates, with a thickness in the range from 20 to $100mm$. The geometry will be almost identical to the Babar IFR. The main difference will be given by the overall thickness of steel of SuperB w.r.t. Babar.
The Babar barrel counted on an overall thickness of 650 mm for the barrel and of 600mm for the endcaps, while the overall thickness of the steel in SuperB should be upgraded to a design value of 920mm, to increase the particle identification capability of the flux return.
Inside proper slots of the flux return will be lodged from 8 to 9 layers of scintillator, w.r.t. the 17 layers of detectors present in Babar. The first layer of detectors is at inner radius w.r.t. to the first steel plate and the last layer will be at outer radius, thus inside the steel only 6 or 7 slots will be needed to lodge the detector planes (see fig. 1.2).
In order to minimize the cost, the baseline design foresees the reuse of all the Babar structure, which has got 17 slots for detectors, and increase the steel thickness inserting metal plates in those of the 17 slots that are left empty. The nominal thickness of each detector plane, composed by two perpendicular layers of scintillators and a box containing them, is of the order of 25 mm, while the gap width of the Babar wedges and doors have nominal dimension between 30 and 35 mm.

The 10 or 11 gaps not used by scintillators will be filled with metal plates. To reach the 920 mm of design value there are 270 mm missing from the Babar parts in the barrel, thus the gaps should be filled with plates of 25 mm in
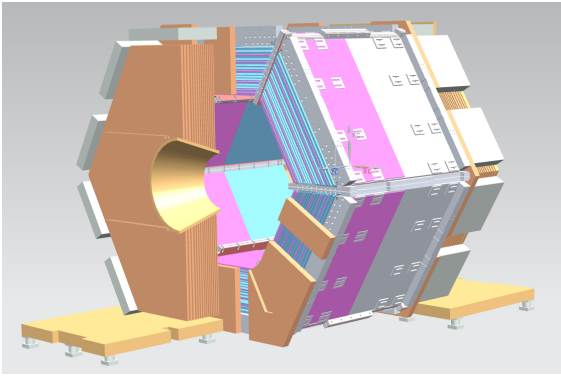
Figure 1.1: The IFR flux return structure.

the more comfortable case and 27 mm in the worst case. According to preliminary measurements, performed in the barrel gaps of Babar, 25 mm plates should fit in all the barrel, apart maybe one or two gaps of the lower sextant, where plates of 25 mm could require forced insertion. The insertion of plates of 27 mm is probably not feasible or could imply a difficult insertion of large part of the plates, with negative impact on the cost and timing of the operation. The baseline idea for the barrel foresees then the use of 25 mm thick metal plates that allow to reach 925 or 900 mm of overall metal thickness, depending on the number of detectors layer that will be defined, 8 or 9.
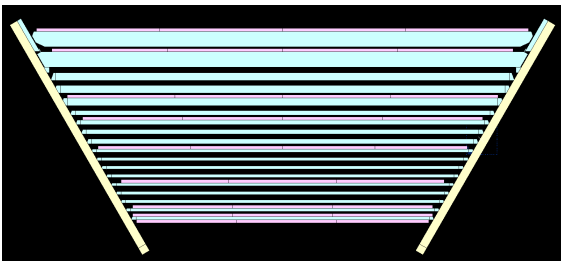
Figure 1.2: Front view of a sextant of the barrel.

For the doors the amount of steel can reach, by fitting the unused gaps, a thickness 50 mm smaller than the barrel, thus 850 or 875 mm of overall metal thickness. The doors geometry allows to increase their overall thickness by adding metal plates on the outer face, as it

was done in the forward doors of Babar, where a plate of 100mm (4 inches) was added, on the outer face, to increase the shielding w.r.t background. This additional plate can also be reused in the SuperB, reducing the need of insertion of plates in the forward doors to 7 gaps, thus 175 mm of overall thickness of plates to be inserted in order to reach the nominal thickness of 920 mm.

In the backward door the addition of an external plate 100 mm thick is not compatible with the presence of the horsecollar as it limits the movements needed for the opening and closing of the doors, then the thickness that can be added on the outer side of the backward door must be minimized. In this case the filling of unused gaps allows to reach an overall thickness of 850 or $875mm$, thus 45 or 70 mm steel plates will be added on the outer face.

In order to define the maximum thickness that can be added on the outer face of the backward door, the opening movements of the doors must be detailed and actual dimensions of the horsecollar must be measured.

The metal composing the plates to be inserted in the unused gaps should match the following criteria:

- Non magnetic material in order to avoid increasing of magnetic forces on the coil

- small interaction length

- acceptable flatness

- convenient cost

In Babar a few layers where filled with brass plates, but nowadays this choice would be very expensive due to cost of copper, strongly increasead in the last years. The choice might then be stainless steel 304L with certified low magnetic permeability. A reasonable value of permeability, low enough to avoid affecting magnetic field and increasing cost only for a few percent, is a relative magnetic permeability < 0.02. Further simulations of the IFR will be performed to determine if all plates need to

be stainless steel or the outer layers (far from the interaction region) could be magnetic, with acceptable effect on magnetic forces. The use, even partial, of standard magnetic steel (similar to the steel used for the present IFR) would reduce strongly the cost of the upgrade.

Another difference of the SuperB IFR w.r.t BaBar, will be in the connection between the barrel wedges and the outer frame (cradle and arches). As in SuperB the willing is to realize the last detector layer outside the wedges, a useful gap for detectors will be realized in between the structure and the wedges, reducing as much as possible the need of connection between the two parts. The connections will be made only at the corners of the wedges leaving available most part of outer wedges top surface to lay down scintillators. This will imply that all the involved parts (cradle, arches, outer wedges) will be modified in a workshop in order to modify the relative coupling.

The increasing of thickness also imply an increased weight of the overall structure, and on top of that, the reduction of connections between outer structure and wedges reduces the strength and stiffness of the overall steel body. Thus the overall deformation of the structure will be verified in detail to crosscheck that stresses are not critical and deformations are compatible with the overall precision needed for such experiment.

Preliminary offers for fitting the gaps of Babar with stainless steel plates 25 mm thick are around 1MEuro. The cost of shipping from US to Italy shall be added, about 0.5 MEuro, while import taxes and duty are assumed to be negligible. Modifications to cradle, arches and outer wedges are required in order to allow the outer layer of detectors, thus the overall cost of the Flux Return in case of reuse of Babar IFR should reach the order of 1.5 - 2 MEuro.

1.2.2 The Active Detector Choice

Calabrese (1 page)

The active detector choice

General layout

1.3 Backgrounds

1.3.1 Main background sources

Machine related background is one of the challenges for the SuperB detector and the background considerations influence several aspects of its design. The IFR detector has been simulated using SuperB FullSim based on GEANT4 and Bruno see Sec.[]. The results of these simulations show that the primary source of background are: radiative BhaBha events, Touschek scattering, pair production, beam-gas scattering and photons from synchroton radiation for a detailed description of the background sources see Sec.[].

Among of these background sources for the IFR detector the dominant one is due to the radiative BhaBha events as will be explained later.

All these background sources produce a high-energy primary $e^{\pm}$ or γ that strikes a beam line element within a few meters of the IP and shower secondaries that can be charged or neutral particles with energies ranging from sub-MeV to several tens of MeV. These particle hit the IFR and may affect the detector performances and speed up the photodetectors aging.

1.3.1.1 Neutron Background

In this context there is a not negligible production of neutrons via giant resonances formation [7]. The neutrons produced with this mechanism have energy of some MeV and they are moderated by the interaction with the detector material, they scatter back and forth on the nuclei both elastically and inelastically losing energy until they come into thermal equilibrium with the surrounding atoms. At this point they will diffuse through matter until they are finally captured by a nucleus. For this reason the neutron energy spectrum in the SuperB environment has a very wide range as shown in Fig. 1.3 where the neutrons are classified according to their kinetic energy.

Since the neutron spectrum has so different range, and the interaction with the matter
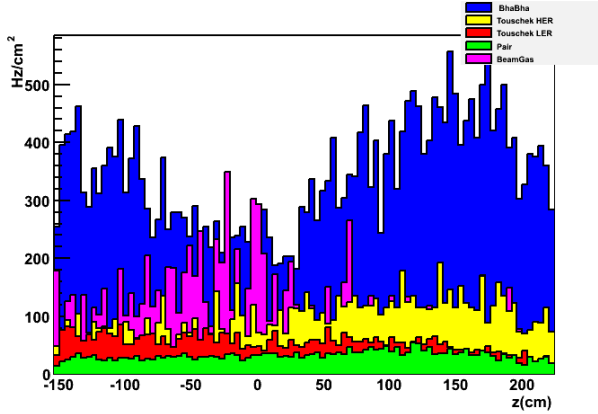
Figure 1.4: Neutron rate on IFR Barrel Layer 0 due to different background sources, the rates are normalized to 1MeV equivalent [8] .
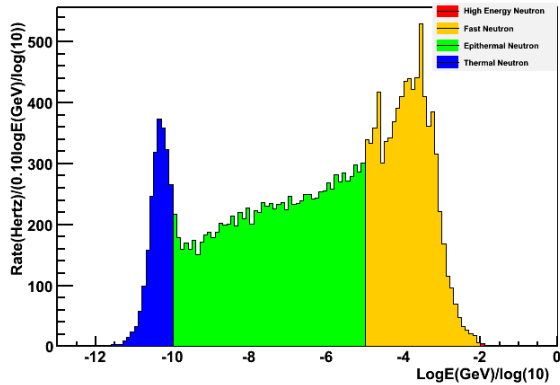
Figure 1.3: Neutron energy spectrum on IFR barrel, the neutron are classified according to their kinetic energy range as high energy neutron, fast, epithermal or thermal.

strongly depends on it, it is standard to characterize the neutron fluence from a source in terms of an equivalent mono energetic neutron fluence because the way as neutron interact has a strong dependency on its energy for additional details see. [8], [9], [10]. For this reason all the neutron rates in this section are normalized to the equivalent of a 1 MeV neutron .

The neutron background not only contribute to the radiation dose of the IFR detector but it is particularly dangerous for the SiPM, the devices used for the detector readout, since they are quite sensitive to radiation, infact if they are exposed to an integrated fluence as high as $10^{11} n_{eq}/cm^2$ (n_{eq} is the equivalent number of 1 MeV neutrons on silicon) they can be severely damaged (i.e. loss of efficiency, increasing of dark current and rate [11]). In Fig. 1.4 is shown the neutron nate on the layer 0 of the Barrel due to the different background sources, the rates are normalized to 1 MeV equivalent as explained above, and they include a *safety factor* that takes into account the fact that the simulation may not reproduce perfectly the reality.

As seen in Fig. 1.4 the main background source is due to the Radiative BhaBha as discussed previously. The rate on Barrel layer 0 corresponds to a *** $neutrons/cm^2$ for a year, these rates are acceptable for a 10 year Super$B$-run and they are the results of a complex shielding system described on Section 1.3.2.

1.3.1.2 Charged Particles

The background due to charged particles is particularly interesting since it can affect directly the detector performances, since it can give fake signal in the detector and affect the track reconstruction and consequently the muon ID. In Fig. 1.5 is shown the rate for electrons and positrons coming from different background sources, as for the neutron the dominant source of the background are radiative BhaBha events. The rate shown in Fig.1.5 are for a electron energy deposited ***¿ MeV that is the nominal threshold we have chosen for the detector.

A high proton rate is observed in the IFR, these protons are produced inside the scintillator in the reaction (n,p) in which the neutron is captured by the scintillator material and a proton is emitted. The cross section for this process falls as 1/v so it is more likely to happen when the neutron has low energy, the resulting proton has a very low energy and for this reason the corresponding deposited energy is low and does not produce signal in the detector for this reason this rate can be neglected.
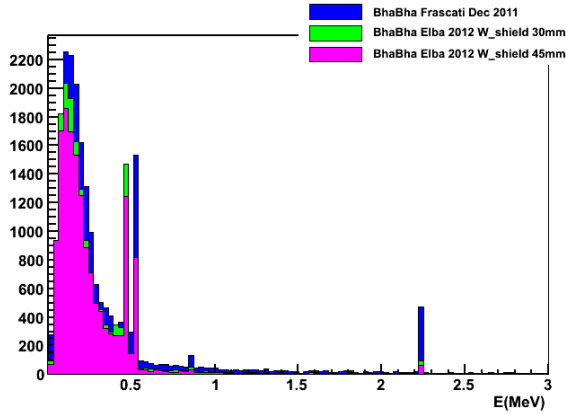
Figure 1.6: Photon energy spectrum for IFR Barrel Layer 0 .
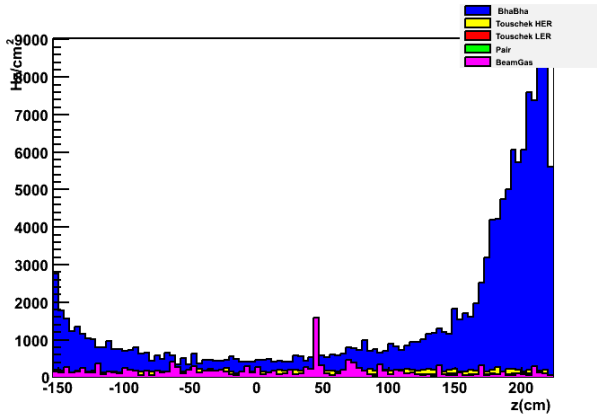
Figure 1.7: Photons Rate on IFR Barrel Layer 0 due to different background sources.
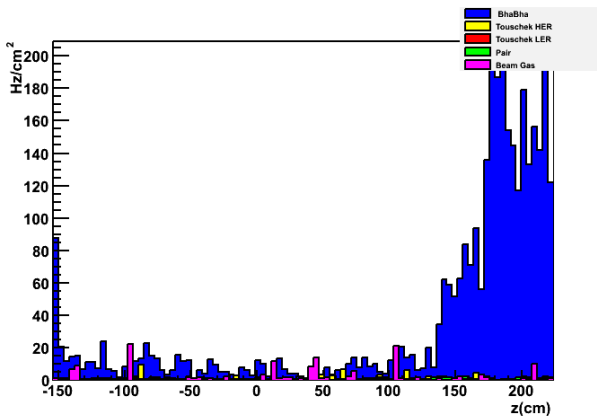
Figure 1.5: Electron rate for the IFR Barrel layer 0 due to different background sources the threshold for the deposited energy is *** MeV .

1.3.1.3 Photon background

All the background sources come from QED events for this reason we studied also the background contribution coming from the photons. The photon energy spectrum has a very broad energy range as shown in the plot of Fig. 1.6 the lines due to neutron capture on Hydrogen (2.223 MeV), due to annihilation radiation (0.512 MeV) and to the neutron capture on B^{10} (0.48 MeV) (the B^{10} is used for radiation shielding see 1.3.2) are clearly visible.

Concerning the IFR the photon rate contribute only to the radiation dose on the scintillator and the contribution given by the high energy photons that convert is already taken into account in the rate of charged particles. The rate for photons on layer 0 of the barrel is shown in Fig. 1.7 and even if it is high it is not expect to affect the detector performance.

1.3.2 Background remediation

All the rates shown on the previous section are the result of a complex shielding system mainly implemented to reduce significantly the number of neutrons crossing the IFR, adding shielding material has also the effect to reduced the electron and photon rate. We implemented a shielding system to the external structure of the IFR and a inner shield to protect the IFR layer 0. The shields are made of Polyethylene $((C_2H_4)_nH_2)$, Boron Loaded (5%) since the polyethylene has a high hydrogen density which slows neutron particles down so they can be absorbed by the Boron since one of the isotope, that compose the natural Boron, the B^{10} has a very high cross section for neutron capture. This shielding design implemented in the Super$B$ Full Sim worked very well since it has reduced the neutron rate of one order of magnitude.

1.3.3 Radiation doses on the IFR detector

1.4 Identification Performances

1.4.1 Muon Detection

Muons are identified by their penetration range in the iron. Above 1.2-1.5 GeV, depending on the incident angle, muons penetrate all layers. Non penetrating muons can be identified from the measured range. More generally, pions separation is reached through a combination of range and hit pattern designed to identify the pion hadronic interaction.

In the SuperB baseline design the iron from BABAR will be reused, so many design parameters are fixed. The main important question the simulation should answer are already outlined in the *CDR*:

- total amount of iron;

- number of active layers;

- size of the scintillation bars;

The SuperB full simulation **??** based on GEANT4 is used to properly simulate the detector geometry and the interaction of the particles with the elements of the detector geometry.

The data taken using the IFR prototype have been used to validate the simulation, in particular the algorithm of digitization needed to generate actuall hits from the hits generated from GEANT4 (gHits). Look at the prototype data analysis section **??**.

In the following, the studies of the detector performances, will be based on the simulation with the prototype geometry, not of the actul detector. In the final version, all the plots and numbers, will be obtained using the SuperB full geometry.

As already outlined before, the criteria for distinguish muons from hadrons is based on the different interaction with the matter: muon track typically release just one hit in each layer, while hadrons can interact strongly in the iron,

generating a hadron shower with several lower momantum particles, producing multiple hits per layer. It is also possibile that few neutrals (neutrons) are produced in the hadronic interaction, thatcan travel long distance before release an hit. In general for pion tracks the number of consecutive active layers is smaller than the muon tracks, on the same time, the average number of hits per each hitted layer is higher than the muons. The hits positions associated with a track are fitted with a second order polynomila function $y = Y(z)$ and $x = X(z)$, where z is the lingitudinal coordinate (layer position) and x and y are the two transverse coordinates given by the hitted scintillator bar. The hit residuals, summed in a $\chi^2 = \sum_{i=0}^{N_{hits}} (Hit(y_i, z_{layer}) - Hit(y_{fit}(z_{layer}), z_{layer}))^2$, are useful to identify the muons as well as the fitted parameters itself. The latter can be compared with the expected direction that comes from the inner detectors to help to suppress part of the contamination from the pion and kaon decays in fly before the first layer of the IFR.

To summarize, we used a consistent set of 10 variables related to:

1. number of hits in the x- and y-view;

2. number of active layers for the x- and y-view;

3. last layer touched, which is transalted in number of interaction length, λ_{int};

4. track continuity;

5. χ^2 of the hits to the tracks for the x- and y-view;

6. parameters of the fitted track.

Distribution of some of the useful variables, as a function of the track momentum, are reported in Fig.1.8. Simple cuts these variables, gives good pion rejection. But the experience from BaBar experiment shows that a multivariate approach gives the best performances on the muon identification even at lower energy when the
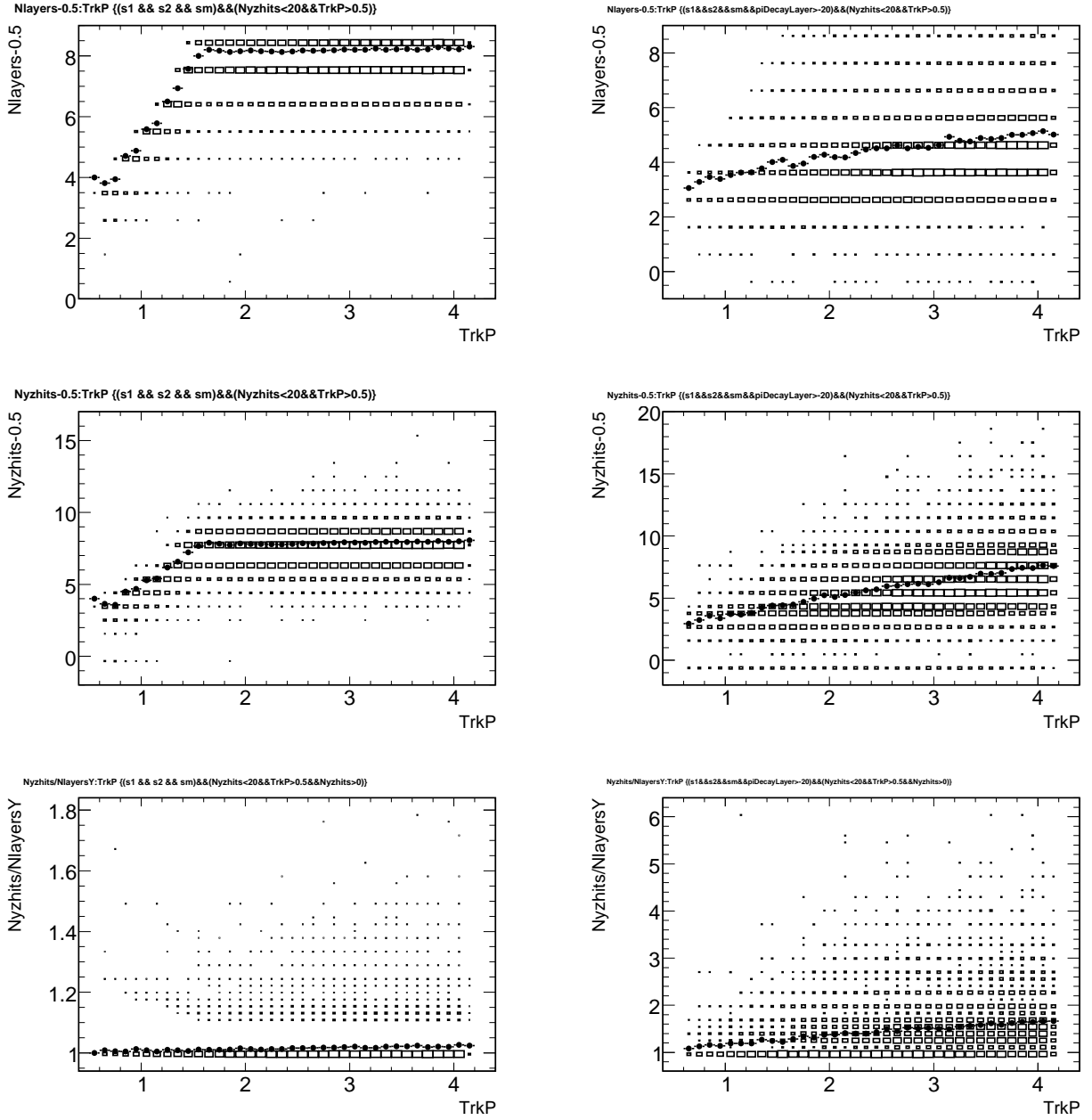
Figure 1.8: Distribution of the number of active layers, total number of hits and average number of hits per active layer, as a function of the particle momentum for μ (left) and π(right). The dots represent the profile of the distribution.

muons stop inside the IFR volume. In particular, because of the correlations between the reconstructed quantity, we used a non-linear multivariate approach like the BDT, which turned out to be very powerful and robust toward sligth changes in the inputs paramaters.

In these studies we did not use some informations that will be available with the full detector. In particular the amount of energy losses in the calorimeter which have slightly different distributions for muons and pions at low energy, can be used to reduce the pion contamination
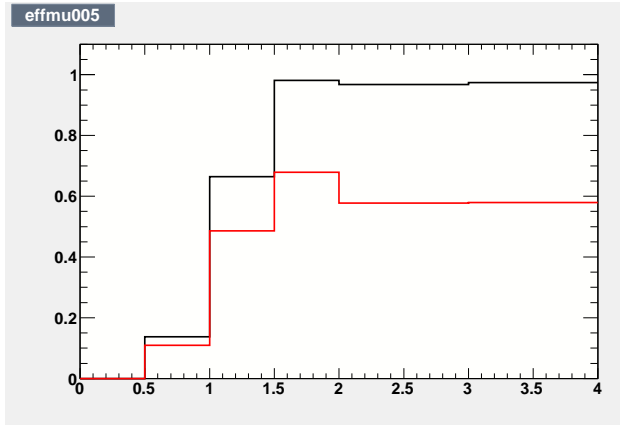
Figure 1.10: Muon efficiency as a function of the momentum, with π mis-id rate fixed in each momentum bin to be 2% (red) and 5% (black).

Table 1.1: Muon efficiency in 5 different bin of momentum between 0.5 and 4 GeV. The muon efficiency are reported with two different requirements on the pion efficiency rate.

P (GeV)	$\epsilon_\mu, \epsilon_\pi = 2\%$	$\epsilon_\mu, \epsilon_\pi = 5\%$
0.5-1.0	?	
1.0-1.5	?	
1.5-2.0	?	
2.0-3.0	?	
3.0-4.0	?	

at low momenta. An the DIRC response that also could help to give informations at lower energy. The signal efficiency - backgroun rejection curves (ROC) are reported in Fig.1.9 just as an examples, in the 1.0-1.5 GeV and 2.0-3.0 GeV range.
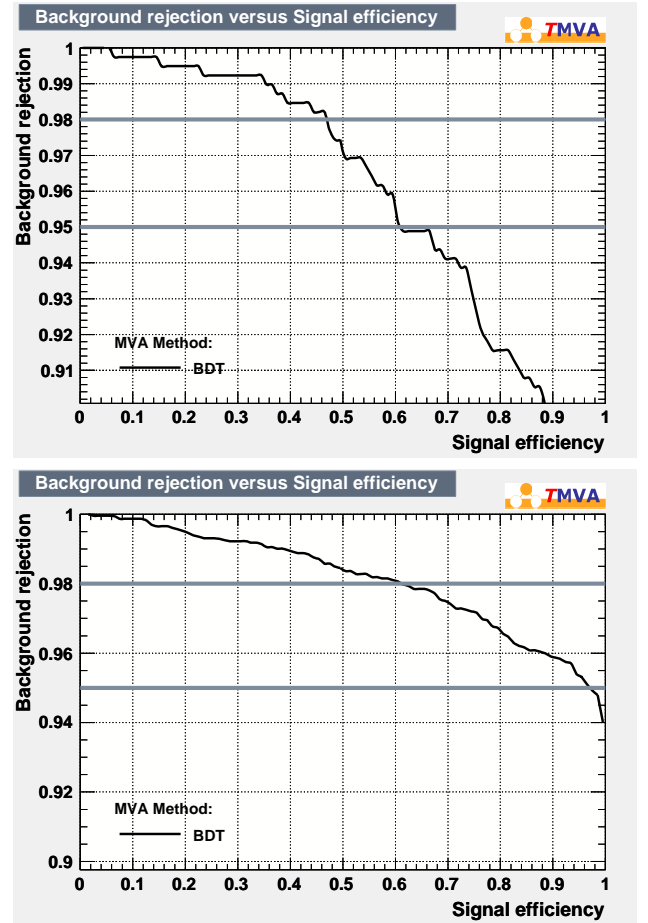
Figure 1.9: ROC curve after the BDT training for muons in the 1.0-1.5 GeV range (left) and 2.0-3.0 GeV range (right). The horizontal line at π rejection efficiency of 95% and 98% are also reported to gide the eyes.

The BDT are trained in different bins of momentum, from 0.5 to 4 GeV. The plot of the muon efficiency as a function of the momentum, with the pi-mis rate fixed at 2% and 5%, are reported in Fig.**??**.

The performances are good and as expected there is a drop in the signal efficiency below 1.5 GeV. The efficiency are reported in Tab.1.1. With the segmentation and granularity studied so far, about half of the pion contamination is due to irreducible background from the π decay in fly.

Rotondo (4 pages)

1.4.2 K_L Detection

Rotondo (3 pages)

1.5 Detector R&D

1.5.1 Module Tests and Results

Baldini, Cibinetto, Montanari (4 pages)

The Active detector technology, described in [?], is the result of an extensive R&D program, carried out in the last years and devoted to the choice of the most effective component for each detector part. In more details, the first studies were mainly dedicated to:

- Scintillators

- Fibers

- Photodetectors

1.5.1.1 Scintillators

Given the large amount of scintillator needed ($\simeq 20$ tons), our attention was attracted since the beginning by the rather unexpensive scintillator produced at the FNAL-NICADD facility at Fermilab (**??**), where the scintillator is produced in large quantities by extrusion and a thin layer of TiO_2 is co-extruded around the active core. This production method suits particularly well our needs to produce long and thin scintillator strips with the desired shape.

We tested a few sample of scintillator strips of external dimensions: $1.0 \times 4.5 cm^2$ (already available at the FNAL -NICADD facility) and $2.0 \times 4.0 cm^2$, considering two options on the positioning of the fibers : fibers placed in an embedded hole or in surface grooves. The difference in light yield has been measured to be a$\simeq 10\%$ higher for the embedded hole option. Since for long bars is very difficult to fill them with the optical glue and given the small difference in light collection, we have chosen the surface grooves as baseline option.

1.5.1.2 Fibers

Since the attenuation length of the scintillator is rather short ($\simeq 35$cm), the light produced by the particle interaction has to be collected using Wave Length Shifting fibers, which brings it more efficiently to the photodetectors. For our application the fibers should have a good light yield to ensure a high detection efficiency for fiber lengths in the range: $\simeq 0.6 - 3\,m$. The

time response was studied as well, since in the first fase of the R& D program also the Time readout option was considered.

We tested WLS fibers from Saint-Gobain (BCF92) [?] and from Kuraray (Y11-300) [?]. Both companies produce multiclad fibers with a good attenuation length ($\lambda \simeq 3.5\,m$) and trapping efficiency ($\varepsilon \simeq 5\%$) but Kuraray have a higher light yield (see fig. 1.11), while Saint-Gobain fibers have a faster response ($\simeq 2.7 ns$ vs $\simeq 9 ns$ for the Kuraray), which ensure a better time resolution.

————– to be discussed
The most effective number of fibers was studied by measuring the light collected with cosmics through 1,2,3 fibers placed on a scintillator bar . As It can be seen on the right plot of fig. 1.11, going from 1 to 2 fibers the gain in light yield is $\simeq 46\%$; going from 2 to 3 fibers the light yield increases by $\simeq 13\%$ with a total gain of $\simeq 65\%$ w.r.t. 1 fiber. So it's not worth to put more that 3 fibers in the scintillator bars. The study is still in progress, to better understand the above behaviour.

————————

Also the possibility of using clear fibers to bring the light signal out of the detector has been studied. As results, we have seen that $10m$ of clear fiber (Kuraray type clear-ps, $\phi = 1.5mm$) reduces, as expected from an attenuation length of $\simeq 10m$, the amount of light by a factor $\simeq 3$ (fig. 1.12). This possibility is desirable since it would allow us to place the SiPMs in a region of the detector where the background radiation flux is lower. It has though many disadvantages: first, in order to have an acceptable amount of light we should use more fibers, and that would increase sensibly the costs; second, the routing of the fibers out of the detector would be very difficult, considering also that the minimum bending radius would be $\simeq 15cm$ for $1.5\,mm$ fibers; third, this solution would require a larger area SiPMs which, in turn, means higher dark noise and faster damage with radiation. Given all these considerations we decided, as baseline choice, to couple the SiPMs directly to the WLS fibres.
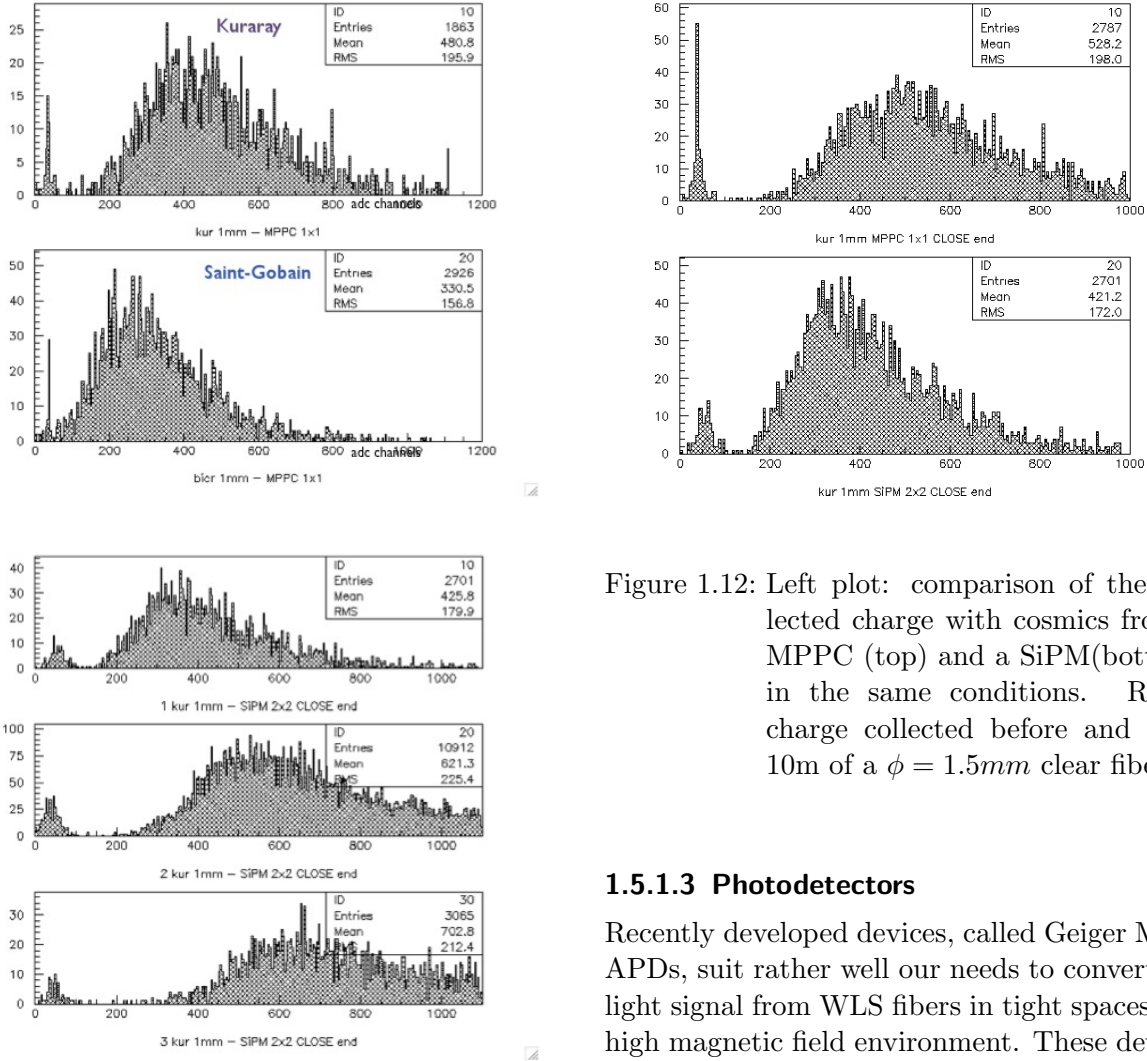
Figure 1.11: Left: light Yield for Kuraray Y11(top plot) and Saint-Gobain BCF92 (bottom plot) fibers.   On the right: comparison of the light yield of 1,2,3 fibers. All the above plots refers to data collected with cosmic rays.
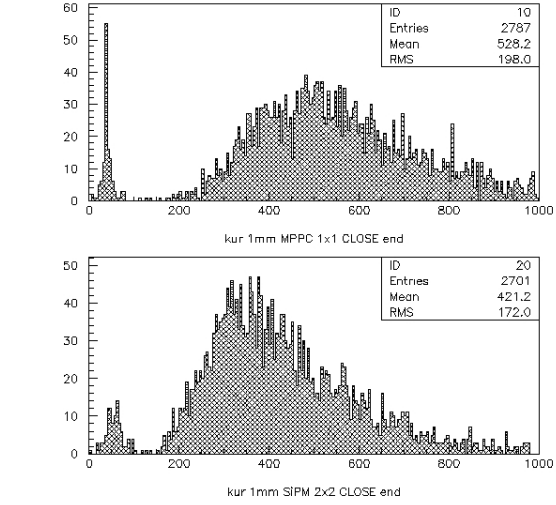
Figure 1.12: Left plot: comparison of the collected charge with cosmics from a MPPC (top) and a SiPM(bottom) in the same conditions.   Right: charge collected before and after 10m of a $\phi = 1.5mm$ clear fiber.

1.5.1.3 Photodetectors

Recently developed devices, called Geiger Mode APDs, suit rather well our needs to convert the light signal from WLS fibers in tight spaces and high magnetic field environment. These devices have high gain ($\simeq 10^5$), low bias voltage ($< 100V$), good Detection Efficiency ($\simeq 30\%$), fast response (risetime$< 1\,ns$), and are very small (few mm^2) and insensitive to magnetic field. They also have a few drawbacks though, like the rather high dark count rate ($few\,100\,kHz/mm^2$ at 1.5 p.e.) and rather sensitive to radiation. At present several companies produce GMAPDs. We concentrated our efforts on the devices produced by by IRST-FBK [?], and MPPCs from Hamamatsu [?].

Our first studies began with $1 \times 1mm^2$ SiPM and MPPCs but, given the low amount of light extracted out of the scintillator, with just one fiber, we soon realized that we would have needed larger devices to couple them with more fibers, while keeping the active surface (and so the noise) as low as possible. Most of our studies were then performed with ($2 \times 2\,mm^2$) FBK devices, since only $1 \times 1\,mm^2$ and $3 \times 3\,mm^2$ MPPCs (too noisy) were available at that time. The comparison between SiPMs and MPPCs showed a lower detection efficiency of the for-

mer (see fig. 1.12) but also a less critical dependence, from temperature and bias voltage fluctuations, of the main parameters like gain and dark count rate. Custom devices from FBK, with a rectangular active area optimized for our needs ($1.2 \times 3.2\,mm^2$, and $1.4 \times 3.8\,mm^2$) were produced and tested for the IFR prototype.

1.5.1.4 Other related studies

Several other studies were performed related to the otimization of the detector performances. The two most relevant are the fiber surface polishing method and the aluminization of the not read-out end of the fiber.

The polishing of the fiber surface was investigated to understand which material and type of blade was optimal to obtain the best quality of the surface (and so the optimal light transmission). We compared the fiber polishing quality for natural and synthetic diamond blades, the tests showed a 10% higher light transmission for the natural diamond option.

Studies have also been performed to cover the free end of the fiber with aluminum (through a sputtering process) in order to reflect back the light, otherwise lost. The result was that the reflection coefficient, with the above technique, is of the order of 50%. We are then considering the possibility to aluminize the free end of the fibers to recover part of the light and to reduce the light yield reduction as a function of the length.

1.5.1.5 New R&D studies...

1.5.1.6 Radiation Damage Studies

SiPMs, as most of the solid state devices, are rather sensitive to radiation. In the superB environment we expect neutrons to be the main source of background, at least at the IFR level. An extensive program, started in 2009 with a first test at the ENEA- FNG (Frascati Neutron Generator) is currently ongoing to understand the effects of intense neutrons fluxes on SiPMs. Following this program, a test on low energy neutrons ($\leq \simeq keV$) has just been carried out at the GELINA (GEel LINear Accelerator) facility in Belgium, and a test with higher energies neutrons is foreseen in the next months.

The first irradiation test was carried out at the Frascati Neutron Generator facility with neutrons of 2.5 MeV [**?**]. As a result, after a dose (1MeV equivalent) of $7.3 \times 10^{10}n/cm^2$, we observed an increase in the drawn current of about a factor 30, of the dark count rate of about a factor 10 higher and a reduction of the average output signal (charge) of approximately a factor 3. While the increase in the dark current is not a major issue by itself, the increase in dark count and the reduction of the output signal might causes a significant reduction of the detection efficiency. This reduction was studied by comparing the SiPM signal from cosmics before and after the irradiation and was estimated to be, in the worst case, of the order of 15%. The
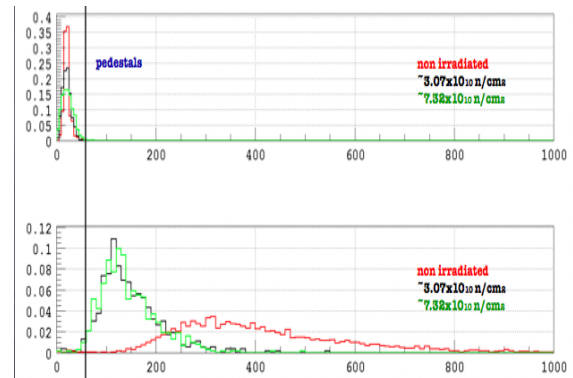
Figure 1.13: Comparison of the cosmic signal distribution before and after the irradiation, for a FBK $1mm^2$ device.

above results are anyway not conclusive. The quality of the SiPMs is fact rapidly improving with time and new tests on recently produced devices (e.g. with an initial dark count rate $\simeq$ factor 10 lower) are needed.

1.5.1.7 New Radiation Damage Studies

this might be included in the prvious paragraph.....
Since an important fraction of neutrons expected at SuperB are in the thermal energies region, a test at the GELINA facility (Geel, BE), where a neutron beam of energy up to a few tens of eV is available [**?**], has been recently carried
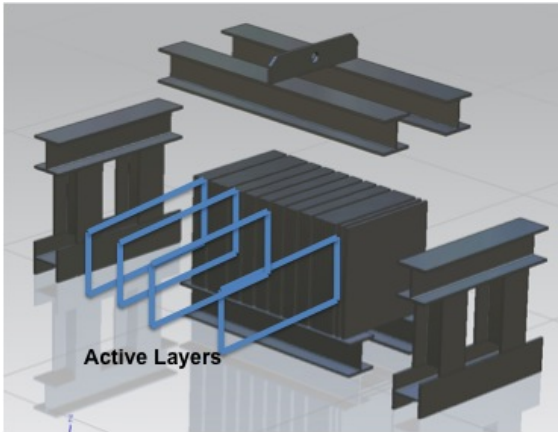
Figure 1.14: The IFR prototype.

Module #	scintillator	Fibers	Photodetectors	Module type
1	2 x 4 cm^2	Bicron, 1mm, L=4.0m	FBK 1.2x3.2 mm^2	TDC standard
2	2 x 4 cm^2	Bicron, 1mm, L=4.0m	FBK 1.2x3.2 mm^2	TDC standard
3	2 x 4 cm^2	Bicron, 1mm, L=4.0m	FBK 1.2x3.2 mm^2	TDC standard
4	2 x 4 cm^2	Bicron, 1mm, L=4.0m	FBK 1.2x3.2 mm^2	TDC standard
5	2 x 4 cm^2	Bicron, 1.2 mm, L=4.0m	FBK 1.4x3.8 mm^2	TDC special
6	2 x 4 cm^2	Bicron, 1.2 mm, L=4.0m	FBK round 1.4mm	TDC special
7	2 x 4 cm^2	Bicron, 1mm, L=4.0m	FBK 1.2x3.2 mm^2 + MPPC 2x2 mm^2	TDC special SiPM/MPPC
8	1 x 4.5 cm^2	Kuraray, 1.2mm, L_x = 110cm, L_y =160cm	FBK 1.4x3.8 mm^2	BIRO standard
9	1 x 4.5 cm^2	Kuraray, 1.2mm, L_x = 370cm, L_y =320cm	FBK 1.4x3.8 mm^2	BIRO standard
10	1 x 4.5 cm^2	Kuraray, 1.2mm, L_x = 190cm, L_y =280cm	FBK 1.4x3.8 mm^2	BIRO standard
11	1 x 4.5 cm^2	Kuraray, 1.2mm, L_x = 210cm, L_y =240cm	FBK 1.4x3.8 mm^2	BIRO standard
12	1 x 4.5 cm^2	Kuraray, 1.2mm, L_x = 210cm, L_y =240cm	FBK round 1.4mm	BIRO special

Figure 1.15: The IFR prototype.

out on a set of more that 20 SiPMs from Advansid, Hamamatsu and SenSL. Fore each device we measured the dark rate and dark current every minute and we regularly ($\simeq$ every hour) performed a I-V curve and a dark rate vs threshold scan. For a few devices we also acquired the dark noise charge spectra. A detailed analisys is ongoing, preliminary results shows that.......

effects of temperature variation.

1.5.2 Prototype Test and Results

Cibinetto

1.5.3 Design and construction of the IFR prototype

Once a baseline design was established, a full depth prototype has been built and tested on

beam at the Fermilab Test Beam Facility **??**, on a muon and pion beam in the range of interest for superB.

The main goal of the beam test was to measure the detector performances: mainly the detection efficiency, the time resolution and the particle identification capability as a funcion of the beam momentum. It was also a very useful test bench to investigate and better understand the assembly strategy and, possibly, to figure out possible issues that might appear during the detector costruction fase.

Fig. 1.15 shows a schematic view of the prototype. It represent a section of $60 \times 60 cm^2$ of the IFR detector, with the full depth, and an iron structure designed to have the possibility of moving the active layers in different positions, in order to change the scintillator-iron segmentation and determine the most effective for particle identification.

A total of 12 active modules, as summarized in fig. **??** were assembled: 4 "standard" for each readout (BIRO and TDC), designed as the baseline technique, and 4 "special" to test the effect of single components (i.e. larger fibers, different photodetector etc...).

Fig. 1.16 shows the general internal structure of an active module of the prototype. The structure is rather simple: two layers of orthogonal 5cm wide scintillating bars, $\simeq 50 cm$ long with 3 fibers housed in surface grooves for each bars. For the TDC modules the scintillator bars were 2 cm thick so a single layer was present. Since the length of the fibers is different on each module, to study the detection efficiency and time resolution in different positions of the IFR detector, the fibers are collected on cylindrical supports and then coupled to the SiPM thanks to custom made plastic (plexiglas) couplers. Their length span from 45 to $370\,cm$ for BIRO readout while are of a fixed length of $4m$ for TDC readout.

The finers are coupled

The front end electronic that provide the bias to the SiPMs, amplifies and discriminates the signals, has been custom designed and is based
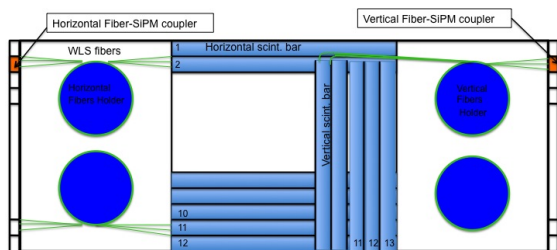
Figure 1.16: Scheme of an active module of the prototype.

on commercial amplifiers (MMIC BGA2748 , BGA 2716). Also the data acquisition and on-line detector control systems have been custom designed specifically for this setup.

1.5.3.1 Beam Tests

Beam Test Setup and data taking. To assess the detection and identification performances the prototype has been extensively tested with a muon and pion beam. The beam was provided by the Fermilab Test Beam Facility at FNAL [cite]; muons and pions is produced by means of a proton beam colliding on an Aluminum target. The particle momentum is selected by two dipoles and has a spread of about 5-10% at 10GeV getting worse at lower momenta. In the momentum range we explore (1-10 GeV) the beam is mainly composed by electrons and pions, with a small fraction <5% of muons. Electrons have been removed by Cherenkov signal used as veto into the trigger. Muon and pions have been selected, above 2 GeV, using another Cherenkov signal; below 2 GeV no external particle identification information was available, so such data have been used only as cross check.

Four beam tests have been performed from December 2010 to March 2012, in each test the apparatus was slightly different due to improvements and lesson learned from previous run, nevertheless the basic concept is composed by (maybe a picture can be useful):

- a slab of 16 cm of iron upstream of the apparatus to "simulate" the material in front

of the IFR detector in the SuperB experiment and to get rid of most of the electrons;

- two or three scintillator detectors with PMT readout placed between the iron and the IFR prototype as trigger;

- the IFR prototype;

- another set of scintillator detectors placed after the prototype to select tracks going through the prototype.

All the PMTs and Cherenkov signals have been acquired with the prototype TDC system in order to refine trigger requests offline.

Table 1.2 shows the data samples acquired at different energies during the four beam tests among with the trigger used.

beam momentum (MeV/c)	min. bias (k evt)	muon trigger (k evt)	pion trigger (k evt)	electron veto (k evt)
1	50	-	-	386
2	60	-	-	236
3	126	134	89	155
4	101	106	76	129
5	262	87	158	25
6	230	218	230	100
8	236	375	413	125

Table 1.2: Beam test data sample.

1.5.3.2 Tests Results

The data from different data taking have been fully analyzed in order to study the detection performances and the muon identification capability of the IFR prototype that will be described in details in the following paragraphs.
In addition to that a first result is about the reliability and the operability of the apparatus: the prototype has been operated for almost forty days of beam test without causing almost any loss of useful data showing that the system design is already mature for a full scale apparatus. The count of lost channels is also very good: we
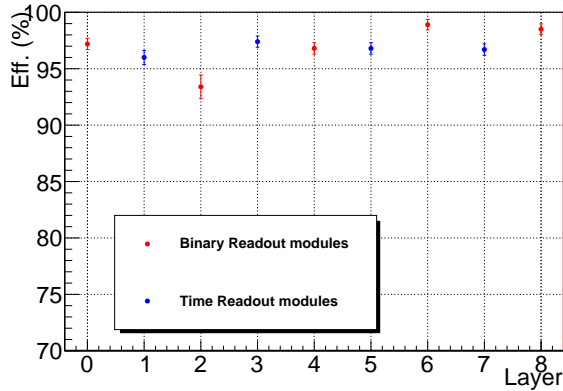
Figure 1.17: Prototype detection efficiency for each layer.
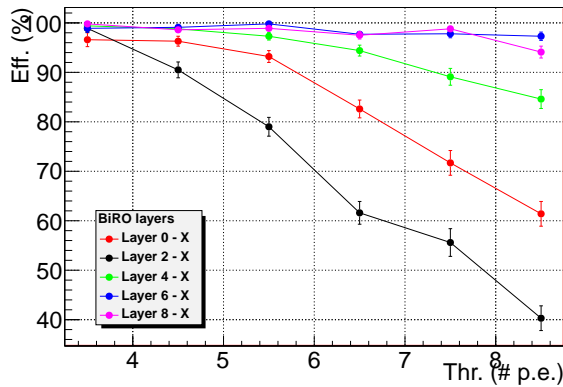
Figure 1.18: Prototype detection efficiency as function of the electronic threshold.

had an infant mortality of just one channel over a total of 237 and after almost one and an half year of testing we end up with three missing channels mainly due to shipping and handling of the detector during the different installations.

Detection Performances. About the detection and track reconstruction performances the main purpose was to confirm the R&D results on a larger scale to assure that the system is capable not only to detect particle hits but to reconstruct three dimensional tracks passing through it. Therefor not only the detection efficiency is a parameter of a paramount

importance, but also the spatial resolution; being the prototype be conceived to test the working principle of the TDC readout option too, the time resolution has been also evaluated.

The detection efficiency has been evaluated using muon events passing through the entire prototype and selected using the backward scintillators. Results are reported i Fig. 1.17 for the binary and time readout modules: the detection efficiency clearly depends on the length of the light path into the fibers that if different from module to module, but in almost any case is >95%. The only exception is for the module in layer number two which has a light path of almost 4 meters, such a long light path will not be present in the final detector design. The detection efficiency depends also on the electronic threshold, Fig. 1.18 shows that, except for the module with the long fibers (layer number two) we have room rise the threshold from the current nominal value, that is 3.5 photoelectrons, to 4.5 (maybe 5.5) with very small efficiency loss. All the results are consistent with the R&D results.

Time resolution performances shown in Fig. 1.19 are also in agreement with our R&D results; the time resolution linearly depends with the fiber length, deviations from the linear behavior are due to SiPM bias voltage overset or underset. The average time resolution is about 1.2 ns and it's enough to guarantee the spatial resolution needed to match the physics performance requirements; on the other hand there is very little space for improvements in the time resolution and moreover the risk of worsening the performances with the aging of the photodetectors.

The last consideration is about the detector occupancy; since one of the main issue of the silicon photomultiplier technology is the dark rate, the noise level has been carefully evaluated both with random trigger and special cut on the time hit. In both cases the average strip occupancy due to the readout is about 1.7%.

Muon Identification Results

Resolution vs Fiber Length
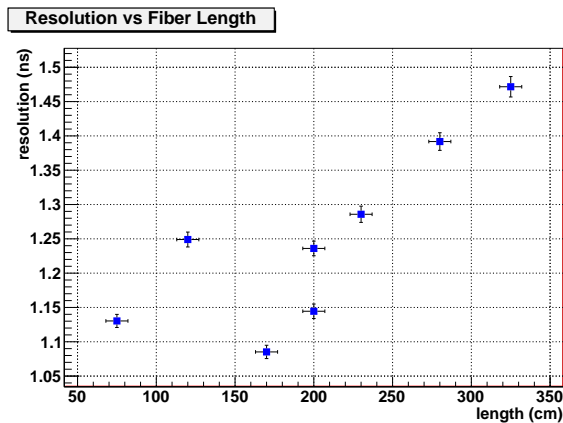
Figure 1.19: Time resolution as function of the fiber length.

1.6 Baseline Detector Design

1.6.1 System Layout

Cotta, Calabrese, Carassiti, Cibinetto (4, 5 pages)

Module concept. Before going into the details of the detector design let's summarize the main points, discussed so far, which have a substantial impact on the overall system layout.

The IFR system must have high efficiency for selecting penetrating particles such as muons, while at the same time rejecting charged hadrons (mostly pions and kaons) in a wide momentum range, from approximately 0.5 GeV to 5 GeV.

The possibility to reuse the BaBar iron offers a cheap solution for the flux return structure, on the other hand it introduces some mechanical constraints which have a significant influence on the detector design: the available space for the detection modules is limited by the dimension of the existing gaps (25mm), and the amount of absorber material is limited to ~ 90 cm of iron. In addition the clarence and path for cables and other utilities is also fixed by the existing structure design.

The other major constraint is due to the machine background that can affect the system by reducing the particle identification performances and speeding up the detector aging.

The maximum rate of charged particle on the IFR detector is located in the forward endcap, close to the beam pipe and, by means of a detailed Monte Carlo simulation, it's estimated to be about xxx Hz/cm^2 decreasing rapidly with the distance from the beam axis; particle identification studies made on the same data sample show that with the current background estimation multiplied by a safety factor the muon ID performances are still acceptable for our system.

For what concern the aging of the photodetectors the main hazard comes from the high flux of neutrons originated by radiative BhaBha background. Recent neutron irradiation tests [cite Musienko] show that SiPM devices continue to work at least up to a dose of $\sim 10^{11} - 10^{12} n_{eq}/cm^2$ but with a considerable increase of dark rate and dark current and an associated efficiency loss of about 80% depending on the cell size. From Monte Carlo simulation we could estimate the neutron flux on the detector that ranges from xxx Hz/cm^2 to xxx Hz/cm^2. We use such information to identify a safe place for the SiPM.

R&D results have proven that, using 1x5 cm^2 (1x10 cm^2) strips, with three fibers for each strip, it's possible to build a detection module 2.5 m (1 m) long having a detection efficiency $> 98\%$ applying a threshold high enough to keep under control the dark count increase due to the neutron irradiation damage. Moreover, beam tests on a large scale prototype has demonstrate the muon identification capability and the reliability of the system.

The K_L^0 identification is also a requirement which has an impact on the detector design. From Mote Carlo simulation and previous experience with the BaBar experiment maintaining
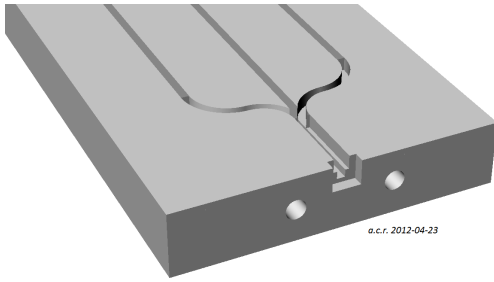
Figure 1.20: a scintillator bar machined to host three WLS fibers, the silicon photomultiplier and the carrier printed circuit board (PCB)

the existing fine segmentation of the three internal layers is enough to retain the the capability to use the IFR

Barrel: number of active layers, channels, geometry.

Endcaps number of active layers, channels, geometry.

1.6.2 Chamber Construction and Assembly

Andreotti, Baldini, Carassiti (3 pages)

module assembly procedure

tooling for module assembly

module QC procedures

1.7 Front-End Electronics

1.7.1 General Overview

Cotta (1 page)

1.7.2 Photodetectors and PCBs

The IFR will exploit extruded plastic scintillators to detect ionizing radiation crossing the apparatus. The light from the scintillators will be collected by embedded wavelength shifting (WLS) fibers and guided to solid state single photon detectors or silicon photomultiplier (SiPM for short). The results of the preparatory R&D activities suggest that three WLS fibers

should be installed in each scintillator bar; the drawing below shows how the plastic scintillator should be patterned to host the WLS fiber.

The baseline design for the IFR detector foresees in fact that the photodetector would be applied at the end of each bar. A printed circuit board (PCB) will be designed to support the photodetector and the miniature connector to a small diameter coaxial cable.

1.7.2.1 Photodetector PCB and optical coupling to fibers

Figures 1.21 shows details of the assembly to be installed at the end of each scintillator bar; the SiPM is first viewed (from the solder pad side) suspended in front of the machined notch where it is lodged once the PCB assembly is installed. The WLS fibers are guided by grooves machined at the scintillator surface; the diamond-cut end of the WLS fibers are positioned flush with the SiPM notch.
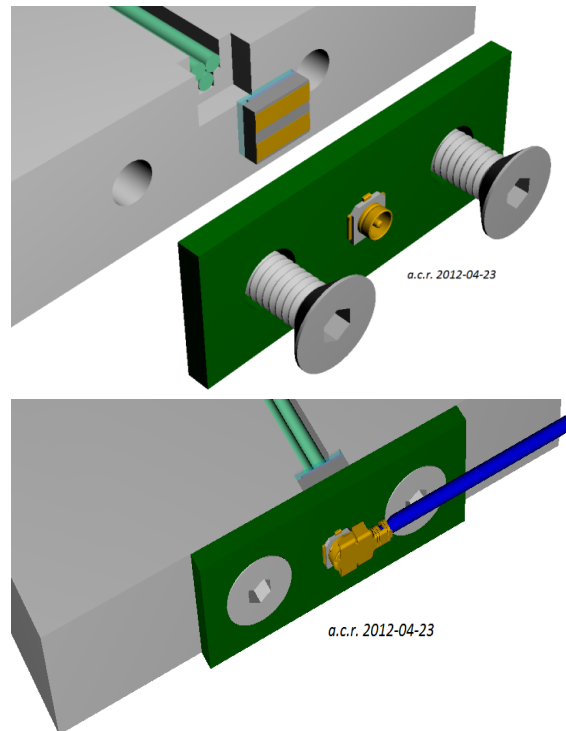
Figure 1.21: details of the three WLS fibers and the PCB for the solid state detector

Figure 1.21 show the assembly in operation: a micro coaxial jack such as the Amphenol A-1 JB, soldered on the PCB, allows the connection of a small diameter coaxial cable; all coaxial cables are routed out of the detector assembly enclosure and reach the front end cards where they are mass-terminated with a high density connector as shown in Fig. 1.22 above.
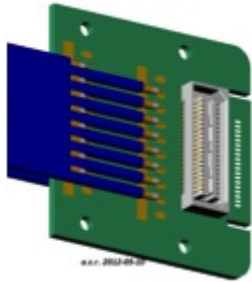
Figure 1.22: a detail of the multi coaxial connector assembly

1.7.2.2 Optical coupling to fibers

As Figure 1.21 shows, the coupling of the WLS fibers to the solid state photon detector is defined by means of machined grooves for the fibers, of a notch for the SiPM and of threaded holes for the PCB mounting screws (and eventually with hole for precision positioning pins). Previous experience with the R&D prototype construction allows to estimate that the relative positions of the fiber ends and the surface of the photodetector can be controlled with a precision in the order of 100um. Optical grease or silicon pads can be used to improve the optical matching.

1.7.2.3 Photodetector location

The scintillator bars, fitted with the photo detectors, will be enclosed in light-tight sheet-metal boxes which will also provide mechanical rigidity to the assemblies (also referenced as modules). Each active layer will actually be composed by a suitable number of modules inserted in the space between two steel plates of the magnetic flux return. It is to be said that once the modules are installed inside the IFR it will be impossible to perform any maintenance

on the majority of them without a major overhaul of the detector; this is especially true for the barrel portion of the detector. Fig. 1.23 below depicts a view of the barrel section of the IFR with a few modules of the innermost layer; the modules envelopes are not drawn, to show the locations of the SiPMs for the barrel; a similar arrangement is foreseen for the active layers of the endcaps. The SiPMs are distributed throughout the entire surface of an active layer and they thus operate in a hostile radiation environment. The solid state photo detectors for the IFR application will thus have to be chosen on the basis of the results of irradiation tests aimed at the evaluation the radiation induced degradation of the photon detection efficiency. This assessment of the radiation tolerance of the SiPM has already been carried out for the devices available at the time the IFR prototype was assembled; more R&D and irradiation test has to be planned before the final SiPM choice is made, to characterize the promising newest generation devices.
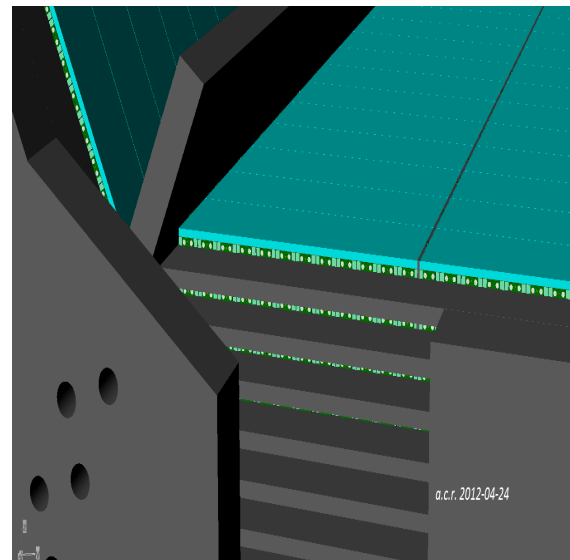
Figure 1.23: Location of the solid state detectors inside the IFR barrel: the detail shows IFR layer 0 detectors belonging to different modules (with the enclosure of the modules removed).

For the modules subject to the highest intensities of background radiation a special layout is also being investigated in which the SiPMs are relocated at more suitable positions by extending the WLS fibers length.

1.7.2.4 Photodetector choice

Different solid-state single photon detectors have been and are being evaluated for the IFR application because the technology is rapidly evolving and it would probably be best to commit to a specific device as late as possible. The devices more intensively tested so far by the SuperB-IFR collaboration are the Silicon Photo Multiplier (SiPM for short) manufactured by the Fondazione Bruno Kessler (FBK) and the Multi-Pixel Photon Counter (MPPC) manufactured by Hamamatsu $[x.7.2_r4, x.7.2_r5, x.7.2_r6, x.7.2_r7]$.

- The key parameters describing the performance of a single photon detector are:

- the photon detector efficiency at the WLS fiber characteristic wavelength

- the fill factor

- the optical cross-talk

- the dark count rate

- the sensitivity of breakdown voltage to temperature variations

- the gain and its sensitivity to temperature variations

The SiPM suited for the IFR application should guarantee a detection efficiency better than 95% when installed in a detector assembly and should present a dark count rate at 0.5 p.e. threshold in the range of a few 100kHz/mm2 at room temperature and nominal bias voltage. SiPM devices satisfying these requirements and maintaining, after irradiation, their performances as close as possible to the required ones will be finally selected for the instrumentation of the IFR detector. Another parameter which will be considered for SiPM device selection would be the availability of detector geometries which would minimize the unused surface area to minimize the ratio dark count rate/ signal rate; for the IFR prototype, for instance, a special device run was commissioned to FBK and devices tailored to the IFR prototype needs were manufactured. The IFR prototype had the majority of the channels equipped with FBK SiPMs but also had channels equipped with MMPCs and both type of silicon photomultipliers performed very well. The final choice will have to be made after more irradiation tests aimed at evaluating the sensitivity of the key device parameters to the type and the dose of the SuperB radiation environment. - Aging and background issues The SiPMs by FBK and the MPPC by Hamamatsu have been irradiated with neutron beams at the Laboratori Nazionali di Legnaro $[x.7.2_r1]$ and at the Frascati Neutron Generator to evaluate the effect of radiation on the devices key parameters $[x.7.2_r2]$.
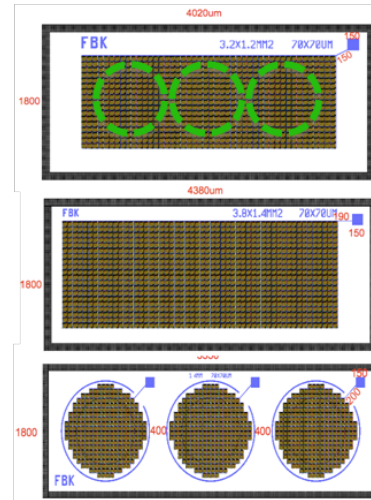
Figure 1.24: the custom SiPM manufactured by FBK for the IFR prototype

These tests showed that for neutron fluxes above a few 10^8 neq/cm2 the dark current and the dark count rate begin to increase while the device gain decreases; after a few 1010 neq/cm2 the efficiency of a cosmic muon detector equipped with irradiated silicon photomultipliers dropped from above 95% to around 75% $[x.7.2_r2]$. A 1MeV equivalent neutron flux of 3^9
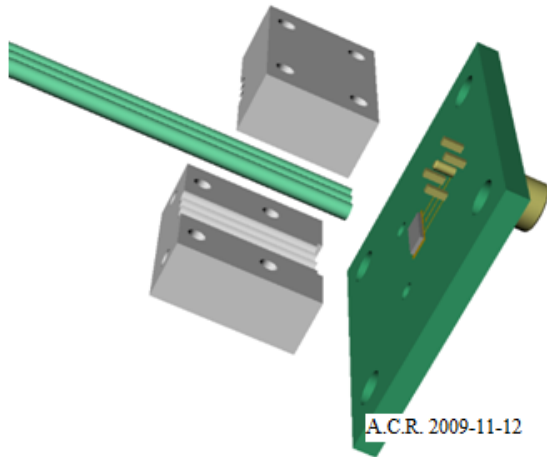
Figure 1.25: a detail of the SiPM carrier PCB
with the MMCX connector

neq/cm2 per year is expected $[x.7.2_r3]$ at the hottest location of the innermost layer of the barrel, for instance. The outcome of the irradiation tests results would seem to advice against installing the SiPM inside the IFR steel, where an eventual replacement would require a major overhaul of the detector and a long down time; on the other hand to position the silicon photomultipliers in accessible locations would require a long clear fiber spliced to the WLS fiber resulting in the loss of the photons available at the silicon photomultipliers, which would also compromise the overall efficiency. Other topics to consider are that the signal processing foreseen for the binary mode readout of the detector is more tolerant of device performance degradation than the timing mode readout formerly considered $[x.7.2_r8]$ and that new silicon photomultiplier devices are being introduced which feature improved radiation tolerance. The dose received by the sensors could also be reduced by multi material shielding layers which would thermalize the neutrons from the beam halo, capture the thermal neutrons and finally absorb the energetic photons resulting from these processes. These considerations lead the IFR collaboration to maintain the baseline design described above, while scheduling more irradiation tests to evaluate the radiation tolerance of the newest SiPMs and the effectiveness of the shielding techniques.

1.7.2.5 Temperature requirements

Silicon photomultipliers operating point and parameters are influenced by temperature. In the case of the IFR detector it is not foreseeable to refrigerate the devices by means of thermoelectric coolers and so we assume that the devices will operate at the temperature of the flux return steel, whose temperature was controlled, in Babar, by means of a chiller system. Rather than control the operating temperature of the silicon photomultiplier devices, the IFR environmental control system will then periodically correct the bias point of each device to compensate for local temperature variations, a technique which was used, as described in Fig. 1.26, in the latest beam tests of the IFR prototypes $[x.7.2_r9]$. The outcome of extensive experiments with the temperature compensation technique is illustrated (see. Fig. 1.26, and 1.27) in the work Compensation of the Temperature Fluctuations in the Silicon Photomultiplier by Wojciech Kucewicz, presented at a seminar in Ferrara in Feb. 2012.
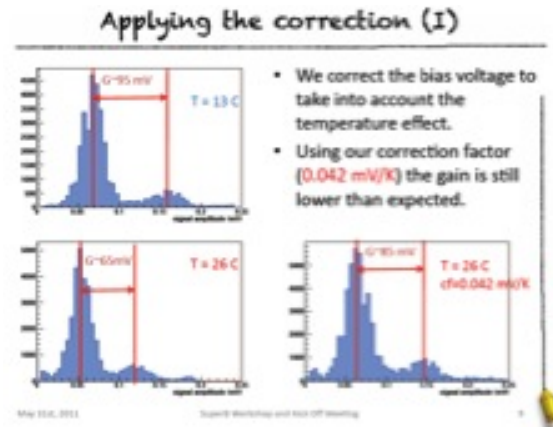
Figure 1.26: compensation   of   temperature-
related SiPM gain shift by bias
voltage adjustments

1.8 Final assembly and installation

Figure 1.27: compensation of temperature fluctuation in SiPM's gain for FBK, SenSL and Hamamatsu devices.
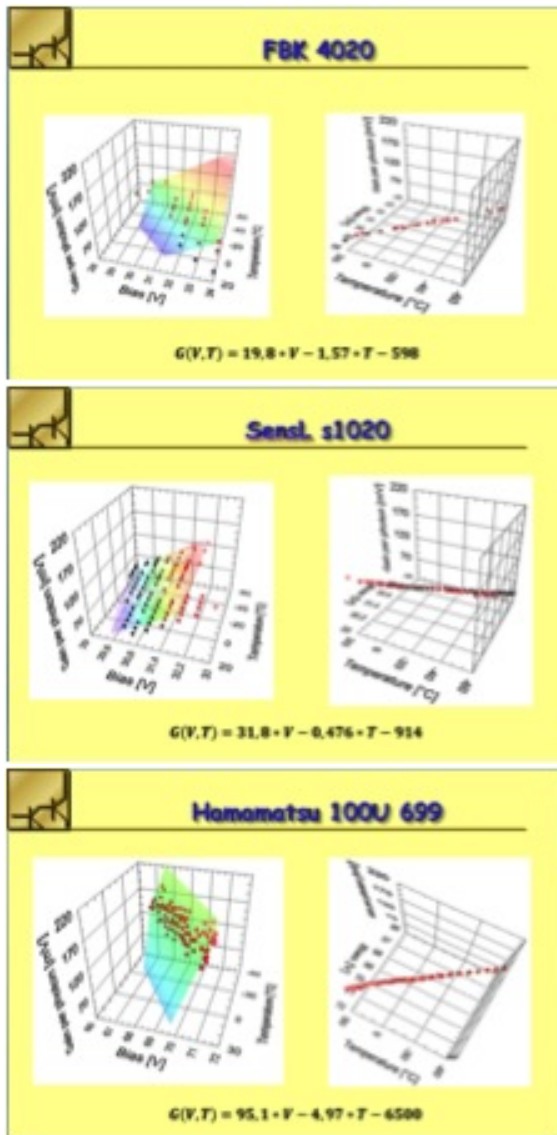
Benettoni, Carassiti (1, 2 pages)

1.9 ES&H issues

1.10 Structure of the IFR group

1.11 Cost and schedule

Bibliography

[1] C. Amsler *et al.* (Particle Data Group), Phys. Lett. B **667**, 1 (2008).

[2] B. Aubert *et al.* (*BABAR* Collaboration), *The BABAR Detector*, Nucl. Instrum. Methods Phys. Res., Sect. A **479**, 1 (2002) [arXiv:hep-ex/0105044].

[3] MINOS Collaboration, *The MINOS Technical Design Report*, NuMI Note, NuMI-L-337.

[4] Bicron specs @ http://www.detectors.saint-gobain.com/fibers.aspx; Kuraray specs @ http://www.df.unife.it/u/baldini/superB/Kuraray.pdf.

[5] C. Piemonte *et al.*, *Development of Silicon PhotoMultipliers at FBK-irst*, Nuovo Cimento **C30**, 473 (2007); MPPC specs @ http://sales.hamamatsu.com/en/products/solid-state-division/si-photodiode-series/mppc.php.

[6] M. Andreotti *et al.*, *A Muon Detector based on Extruded Scintillators and GM-APD Read-out for a Super B Factory*, Nuclear Science Symposium Conference Record, 2009. NSS '09. IEEE(2009).

[7] B.L. Berman, S.C. Fultz, Rev. Mod. Phys. (1975) 713

[8] *Standard practice for Characterizing Neutron Energy Fluence Spectra in Terms of an Equivalent Mono-energetic Neutron Fluence for Radiation Hardness Testing of Electronics*", ASTM E 722 -93

[9] G. Lindstrom *et al.* [ROSE Collaboration], Nucl. Instrum. Meth. A **465**, 60 (2000).

[10] Nuclear Instruments and Methods in Physics Research A 426 (1999) 1?15

[11] M. Angelone *et al.*, *Silicon Photo-Multiplier radiation hardness tests with a beam controlled neutron source*, arXiv:1002.3480 [physics.ins-det].